Geotechnical Testing Journal, Vol. 33, No. 1
Paper ID GTJ102366
Available online at: www.astm.org

J. Y. Lee[1] *and J. C. Santamarina*[2]

Electrical Resistivity Tomography in Cylindrical Cells—Guidelines for Hardware Pre-Design

ABSTRACT: Electrical resistivity tomography (ERT) allows for fast, non-destructive, and efficient sediment characterization and geotechnical process monitoring in the field as well as in laboratory applications. Besides the spatial distribution of resistivity, specimen geometry and electrode configuration determine the electrical potential distribution and the ensuing spatial resolution in the tomogram. We examine potential and current density distribution in various ERT system configurations using both experimental and numerical methods and explore optimal electrode configurations for cylindrical cells. Results show that optimal ERT configurations must take into consideration the required spatial resolution, sensitivity to anomalies, signal strength, and shunting effects along the cell perimeter. The system characteristics are defined in terms of electrode width W_{elec} and length L_{elec}, cell diameter D_{cell}, and the distance from the electrode plane to conductive end-plates δ. The following dimensionless ratios emerge as guidelines for system pre-design: $W_{elec}/D_{cell} \approx \pi/2n$, $L_{elec}/D_{cell} \approx 0.4$, $\delta/D_{cell} \geq 1$, where n is the number of electrodes around the perimeter.

KEYWORDS: electrical resistivity, tomography, electrode, soil, electrolyte, non-destructive testing, geophysics

Introduction

Electrical measurements have been extensively used for in situ characterization and in laboratory studies in a wide range of geotechnical applications mostly to characterize heterogeneities such as porosity and degree of saturation and to monitor geotechnical processes such as multiphase flow in sediments. The most intensive implementation and data analysis of electrical measurements are in the form of electrical resistivity tomography (ERT) or electrical impedance tomography (Zhou et al. 2001; Borsic et al. 2005; LaBrecque et al. 2004; Comina et al. 2008). The main advantages of these systems are the geotechnical relevance of electrical measurements, the non-destructive nature of the measurements, fast data acquisition time, and relatively easy and inexpensive implementation in comparison to other tomographic systems such as X-ray tomography or magnetic resonance imaging.

ERT determines the spatial distribution of electrical resistivity within a specimen from electrical measurements conducted with electrodes placed at the specimen boundaries. A current is injected between the source and sink electrodes by imposing an electrical potential difference between them, and potential differences among the remaining electrodes are measured by pairs. This procedure is repeated by varying the source and sink electrode pairs until a comprehensive data set is obtained. The measured potentials are used to reconstruct the distribution of resistivity within the specimen using inversion algorithms.

Specimen geometry, electrode configuration, and the spatial distribution of resistivity determine the potential distribution and current density within the specimen. Furthermore, the location of electrodes affects spatial resolution and signal-to-noise ratio (Booth and BasarabHorwath 1996). The importance of hardware design has been mentioned by previous research on electrical tomographic imaging. Previous studies showed that (1) peripherally mounted electrodes render low resolution at the center of the specimen (Seagar et al. 1986), (2) the addition of an electrode at the center improves the resolution within the central area (Lyon and Oakley 1992), (3) current injection between adjacent electrodes produces the best local resolution, and (4) current injection between opposite electrodes produces the best signal-to-noise ratio (Avis and Barber 1994).

This manuscript documents a complementary experimental and numerical study conducted to optimize the design of ERT system for cylindrical soil specimens commonly used in geotechnical applications, especially focusing on the electrode configurations for measurement with the best signal-to-noise ratio in view of robust inversion. The study results reported herein are generalized with dimensionless ratios to expand applicability to other cylindrical ERT systems.

Manuscript received February 5, 2009; accepted for publication August 28, 2009; published online December 2009.

[1]Petroleum and Marine Resources Division, Korea Institute of Geoscience and Mineral Resources, 92 Gwahang-no, Yuseong-gu, Daejeon 305-350, South Korea (corresponding author), e-mail: jyl@kigam.re.kr

[2]School of Civil and Environmental Engineering, Georgia Institute of Technology, 790 Atlantic Dr., Atlanta, GA 30332-0355, e-mail: carlos@ce.gatech.edu

Preliminary Studies

In this first section, we explore unique difficulties in the electrical characterization of soils, identify the characteristic ERT signature around a cylindrical experiment, and assess the validity of numerical models against experimental data.

Electrode Polarization—1D Field

Electrode polarization effects develop in electrical measurements in soils due to the ionic conduction in electrolytes. It manifests as a pronounced potential drop near electrodes. The capacitive-type electrode polarization effect diminishes as the operating frequency increases, but it extends into higher frequencies as the conductivity of the electrolyte increases. The frequency range that can avoid the electrode polarization effect is explored experimentally as below.

A latex tube (diameter $D=8$ mm and length $L=250$ mm) is filled with a salt water solution (electrical conductivity

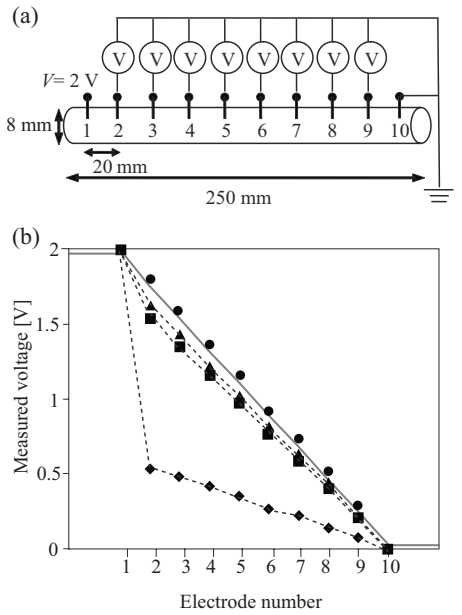

FIG. 1—*Electrode polarization in pseudo-1D configuration. (a) Experimental configuration. (b) Potential distribution at the electrodes. Symbols: Spade, 1 Hz; square, 5 Hz; triangle, 10 Hz; and circle, ≥50 Hz.*

σ_{el}=0.05 S/m) to create a pseudo-one-dimensional (1D) current flow geometry. Ten electrodes are mounted equally spaced along the tube (Fig. 1(*a*)). The source (1) and the sink (10) electrodes are connected to an ac power supply (ΔV=2 V), and the potential at all electrodes is measured with respect to ground. Data gathered at different excitation frequencies are plotted in Fig. 1(*b*). A pronounced potential drop is observed in low frequency data near the source electrodes. This phenomenon is called electrode polarization and results from the incompatibility between ion-based conduction in the electrolyte and electron-based conduction in the peripheral circuit (Santamarina et al. 2001).

The frequency response is similar to a capacitor (charging at the fluid-metal interface) in series with a resistor (the medium). Electrode polarization and the associated capacitive impedance vanishes at high frequency. Data in Fig. 1(*b*) show that an excitation frequency higher than 50 Hz is required to obtain the linear response $V=f(x)$ expected in the 1D system. In general, electrode polarization effects extend into higher frequencies as the conductivity of the electrolyte increases (Klein and Santamarina 2003; Santamarina and Fratta 2003). The conductivity of fresh water-soil mixture can be much lower than 0.05 S/m, but those of marine sediments can range up to 3∼5 S/m. Therefore, high frequency operation range, probably 1–10 kHz, is recommended unless a similar calibration study and frequency sweep experiment data prove otherwise.

Potential Drop near Source and Sink Electrodes in Three-Dimensional Fields

The second experiment is designed to examine geometric Laplacian effect on electrical distribution and consists of a cylindrical specimen geometry. Sixteen point electrodes (electrode width W_{elec}=1.1 mm and electrode length L_{elec}=1.1 mm) are mounted equally spaced around the perimeter of the plastic cylinder (diameter D=60 mm and height H=60 mm; Fig. 2(*a*)). The cylinder is filled with a salt water solution (σ_{el}=0.05 S/m) same as the 1D case. The opposite-electrode excitation scheme is used: The applied potential difference between the source (1) and the sink (9) electrodes is 3.5 V, and the selected operating frequency is 1 kHz, which is high enough to avoid the electrode polarization. The sketch in Fig. 2(*c*) and results in Fig. 2(*d*) show a significant potential change near source and sink electrodes. The high potential changes near the source and the sink diminish the system response to the characteristics of the soil. However, these are not due to electrode polarization (f=1 kHz), but due to the geometrical electric field spreading, there is a high concentration of equipotential lines near the source, and the sink electrodes as can be seen from Fig. 2(*c*). The selection of the applied potential difference reflects the competing requirements between resolution (high applied voltage preferred) and non linear effects at high current densities (low applied voltage preferred).

A parallel numerical study is implemented using a commercially available three-dimensional (3D) finite element code (COMSOL Mulitiphysics) to corroborate the distribution of the potential in this configuration. We reproduce the same geometry as the physical model shown in Fig. 2. The outer boundary is set to be nonconductive, the conductivity of the stainless steel electrodes is fixed at $\sigma_{el}=4\times10^{6}$ S/m, and the conductivity assigned to the electrolyte is the measured value of σ_{el}=0.05 S/m. Numerical simulation results are superimposed on experimental results in Fig. 2(*d*). There is close agreement between experimental and numerical results (difference of ≤0.3 % in all values). Results highlight the predominant effect of electrode geometry on the distribution of the potential near sink and source electrodes. The characteristics shape of the response signal suggests that all the information should be extracted from the small potential difference measured at intermediate electrodes 2–8 and 10–16.

Electrode Size

The pronounced potential changes near the source and sink electrodes 3D system configurations leave a small potential difference between measurement electrodes, reducing the sensitivity to anomalies and signal-to-noise ratio (see also Pinheiro et al. (1998)). We attempt herein to reduce the high current density near small electrodes and associated high potential change by using wider electrodes (a similar strategy is reported in Huaxiang et al. (2001)). The cell configuration is the same as in Fig. 2, but we vary the width W_{elec} and length L_{elec} of the source and sink electrodes. Plots a and b in Fig. 3 show the electrical potential profiles measured around the perimeter of the cell, and plots c and d show the potential at electrodes 2 and 8 closest to the source (1) and the sink (9). Results clearly show that wider and longer electrodes reduce the potential change near source and sink electrodes, suggesting less current density near source and sink (see additional evidence in Newell et al. (1998)). The asymptotic values shown in Fig. 3(*c*) and 3(*d*) is the potential at the electrodes when shunting take place, i.e., when the current concentrates along the high conductivity perimeter created by contiguous electrodes and bypasses the specimen: The upper asymptote is at 7/8 V_o and the lower one is at 1/8 V_o.

Large size electrodes reduce the spatial resolution in tomographic inversion (Huaxiang et al. 2001). Ideally, the source and sink electrodes should be as large as possible, while the measuring electrodes should be as small as possible (Pinheiro et al. 1998). However, electrodes are alternately used for source, sink, and measurement electrodes: Hence size-related trade-offs should be properly

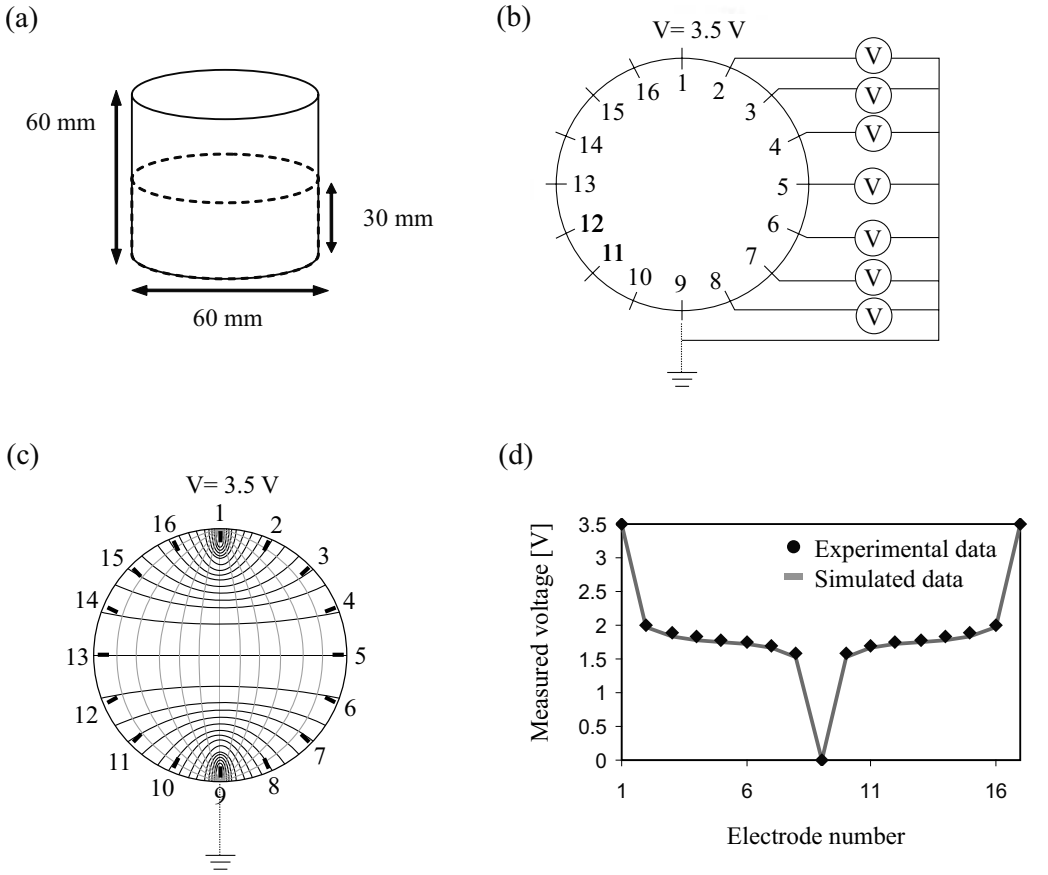

FIG. 2—*Electrical potential distribution around a cylindrical specimen. Geometric Laplacian effect without electrode polarization (f = 1 kHz and W_{elec} and L_{elec} = 1.1 mm). (a) Cell geometry. (b) Circuit. (c) A sketch of the equipotential line distribution. (d) Results.*

considered in advance. The optimum ratio of electrode dimensions to specimen dimensions and boundary effects are studied next in the context of a cylindrical cell.

Electrical Resistivity Tomography Cell for Geotechnical Studies

A stainless steel thick-wall cylindrical cell is built to conduct high effective stress and high pore fluid pressure sediment characterization and process monitoring under zero lateral strain k_o conditions (internal cell diameter D_{cell}=60 mm and length L_{cell}=152.4 mm). The cell is sketched in Fig. 4.

The ERT system under consideration consists of an eight electrode per plane configuration. Electrode size and insulation requirements are studied using numerical simulation (COMSOL Multiphysics). The model geometry and boundary conditions are selected to match the cell. The interface between the specimen and the stainless steel cell wall includes an electrical insulation layer, but there is no insulation coating between the specimen and end caps. The source electrode (1) is set at a 3.5 V, and the sink electrode (5) is grounded in all simulations. Conductivity values are 0.5 S/m (a value for sediments saturated with ion-dissolved water) for the specimen for and 4×10^6 S/m (a value for stainless steel) for the cell and electrodes. The 3D mesh consists of small elements near electrodes and larger elements away from the measurement plane, for a total of 25 068 elements. Model characteristics are shown in Fig. 4. The geometry of electrodes and the medium properties are varied in the parametric study. Details and results follow.

Electrode Width

Two different shapes of electrodes (half-cylindrical and flat) and four different electrode widths (W_{elec}=1.1, 3.2, 6.4, and 12.8 mm) are simulated and sketched in Fig. 5. The half-cylindrical geometries are selected to create the most compatible sink and source geometry for near-electrodes equipotential. In all cases, the electrode length is L_{elec}=7 mm so that the ratio $L_{ele}/D_{cell} \approx 0.11$.

Figure 6 shows that (1) regardless of the electrode shape, the voltage drop near source and sink electrodes decreases as the electrode width increases, and (2) a detailed analysis of numerical results reveals that half-cylindrical electrodes produce a less concentrated potential distribution near the source and the sink electrodes than the flat electrode geometry. The asymptotes shown in Fig. 6(*c*) are the potential at shunting, i.e., 1/4 V_o and 3/4 V_o. Note that no information can be gathered about the medium when shunting takes place.

The effect of electrode width on anomaly detection is examined using a spherical inclusion (inclusion diameter D_{inc}=12 mm and D_{inc}/D_{cell}=0.2) of both high and low conductivity with respect to the host sediment (inclusion conductivity σ_{inc}=0.05 and 5.0 S/m and host sediment conductivity σ_{sed}=0.5 S/m). Four in-plane

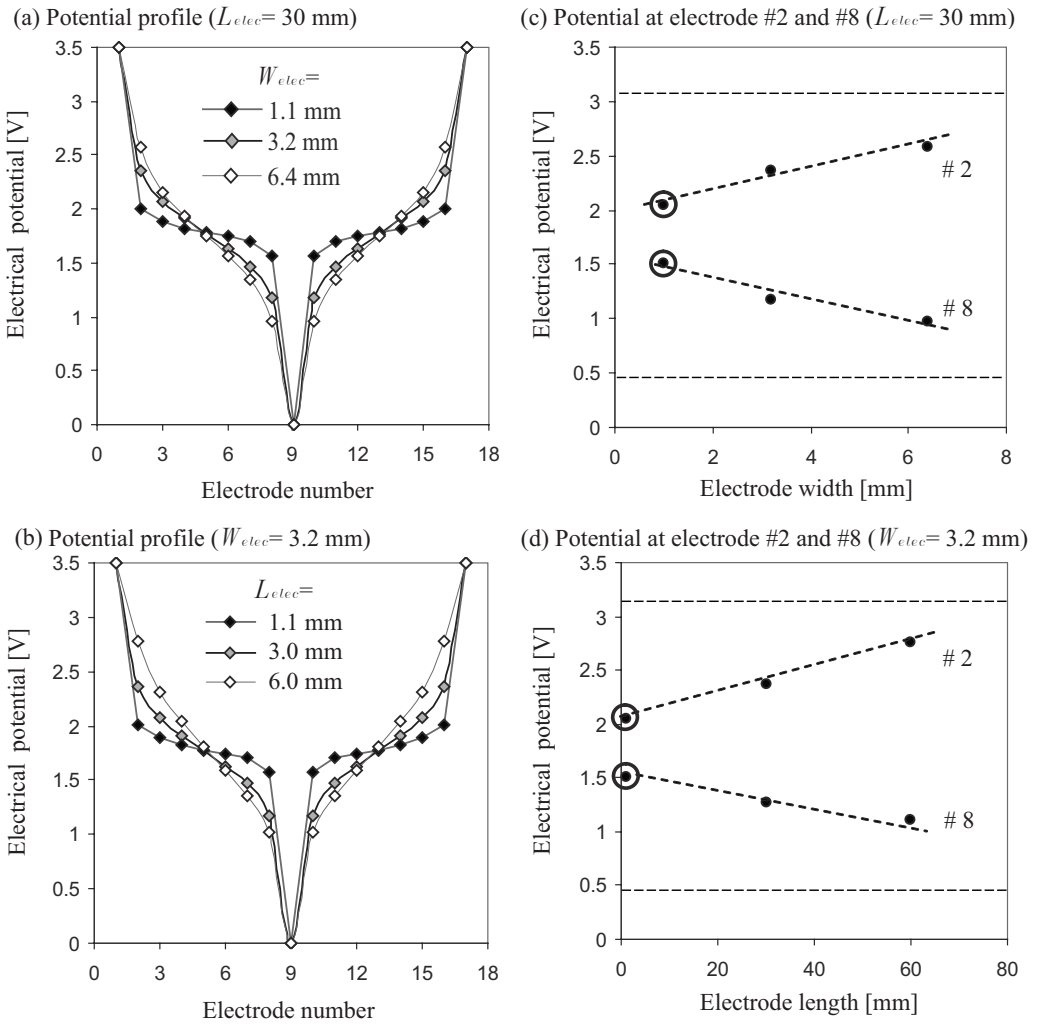

FIG. 3—*Effect of electrode width and length on potential distribution—experimental results. The cylindrical cell in Fig. 2 is used with same source and sink conditions: (a) Potential profile around the perimeter (L_{elec} = 30 mm and varying width), (b) potential profile around the perimeter (W_{elec} = 3.2 mm and varying length), (c) potential at electrodes 2 and 8 (L_{elec} = 30 mm and varying width), and (d) potential at electrodes 2 and 8 (W_{elec} = 3.2 mm and varying length). All potentials are measured with respect to the sink (9) electrode, which is taken as ground. Circled data are from point electrodes*

positions of the inclusions are considered in each case, as shown in Fig. 7: (a) Near the source, (b) near the sink, (c) off-centered in the middle, and (d) centered in the cell. Figures 8 and 9 show the potential change $\Delta V/V_o$ with respect to the corresponding potential measured in the homogenous medium induced by either high or low conductivity inclusions for the half-cylindrical and flat electrodes. The following observations can be made from these results.

— The anomaly response is stronger for wider electrodes.
— Relatively large (D_{inc}/D_{cell}=0.2) and highly contrasting in-

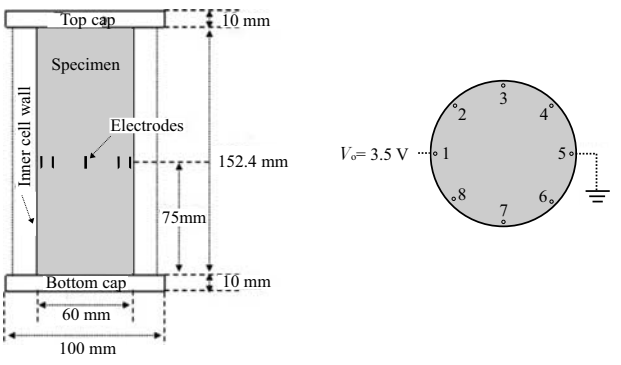

FIG. 4—*Model geometry and measurement configuration in numerical study. Electrode 1 is the source electrode (V_o = 3.5 V), and electrode 5 is the sink electrode (ground).*

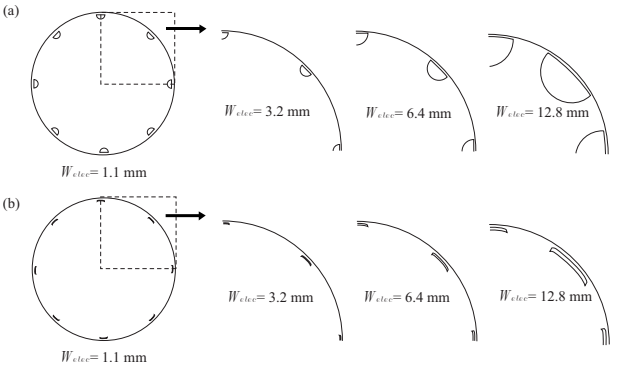

FIG. 5—*Electrode geometries for the study of electrode shape and size effects: (a) Half-cylindrical electrodes. (b) Flat electrodes. The electrode length is fixed at 7 mm. Other model characteristics are specified in Fig. 4.*

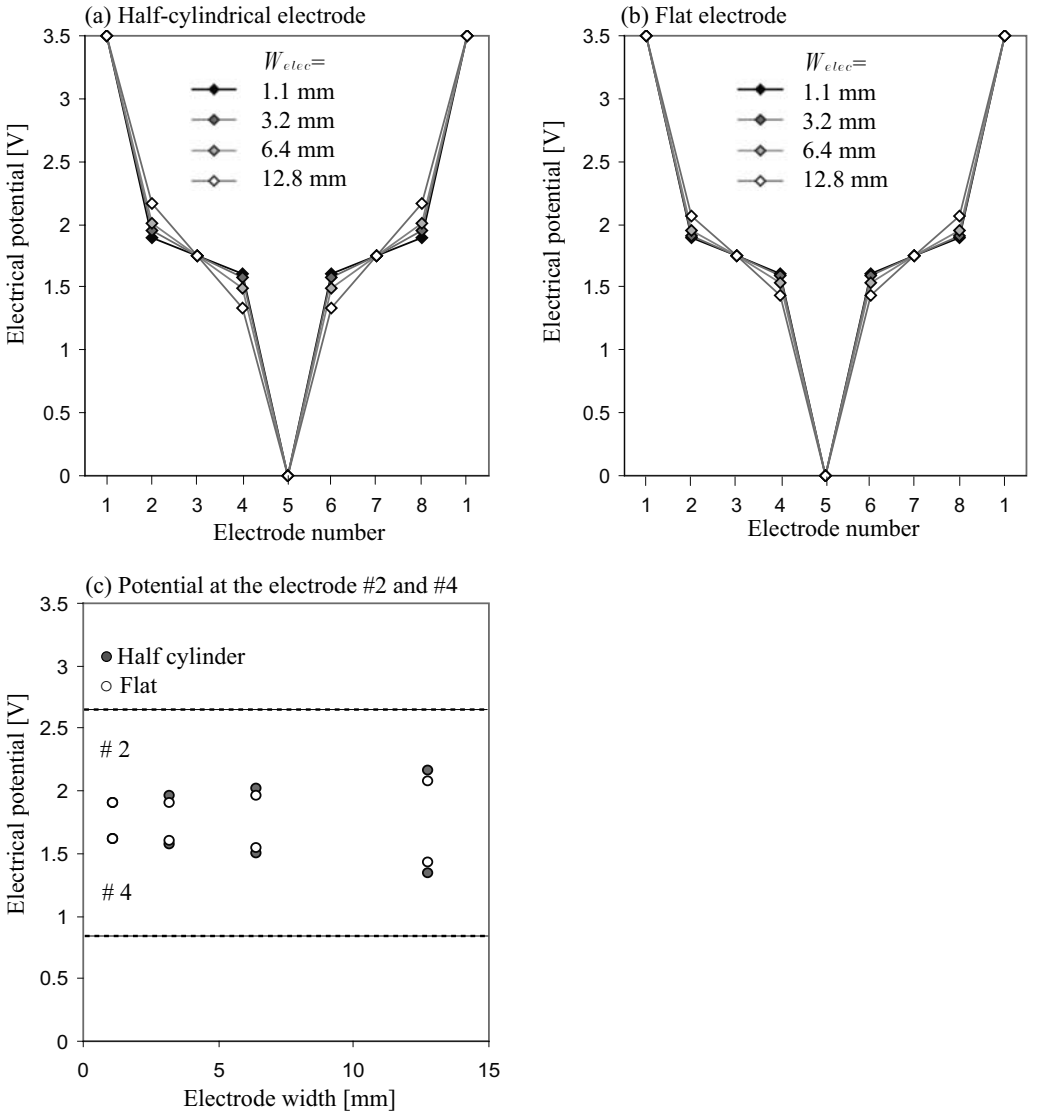

FIG. 6—*The electrode width and shape effect on the measured potential—homogeneous medium. Potential profile for (a) half-cylindrical electrodes and (b) flat electrodes. (c) Potential at electrodes 2 and 4 against electrode width for all simulated shapes and widths. The length of electrodes is 7 mm in all simulations.*

clusions ($\sigma_{inc}/\sigma_{sed}$=0.1 and 10) produce only $\Delta V/V_o \leq 3$ % response even for the widest electrodes (note the proximity to electrodes in Fig. 7).

— Electrodes are more sensitive to conductivity anomalies near the boundary than in the center regardless of electrode diameter and shape (similar results reported in Dickin and Wang 1996; Cohen-Bacrie et al. 1997; Pinheiro et al. 1998).

— The response signal with respect to the homogeneous medium, $\Delta V/V_o$, is slightly higher for high conductivity inclusions ($\sigma_{inc}/\sigma_{sed}$=10) than for low conductivity inclusions ($\sigma_{inc}/\sigma_{sed}$=0.1). Note that "low impedance healing" is observed not only in Laplacian conduction processes but in other phenomena as well, such as in wave propagation (see Potts and Santamarina (1993)).

— Half-cylindrical and flat electrodes show similar response patterns for the various inclusion types and locations, but the signal is stronger with half-cylindrical electrodes. This is in part due to the shorter distance between the inclusion and the half-cylindrical electrodes.

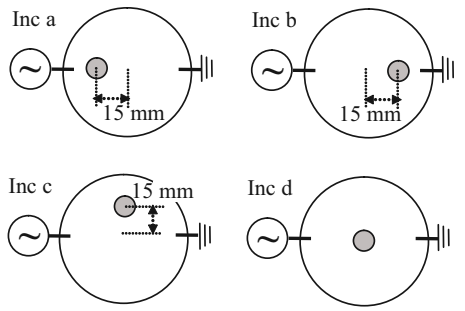

FIG. 7—*Inclusion geometries for the study to identify optimal electrode width in detecting a spherical inclusion (D_{inc}=12 mm and σ_{inc}=0.05 and 5 S/m). Other model characteristics are specified in Fig. 4.*

In summary, half-cylindrical electrodes that are $W_{ele}/D_{cell} \approx 0.2$ provide the highest sensitivity to the presence of conductivity anomalies in cylindrical cells with eight in-plane electrodes. Clearly, narrower electrodes must be used when a higher number of

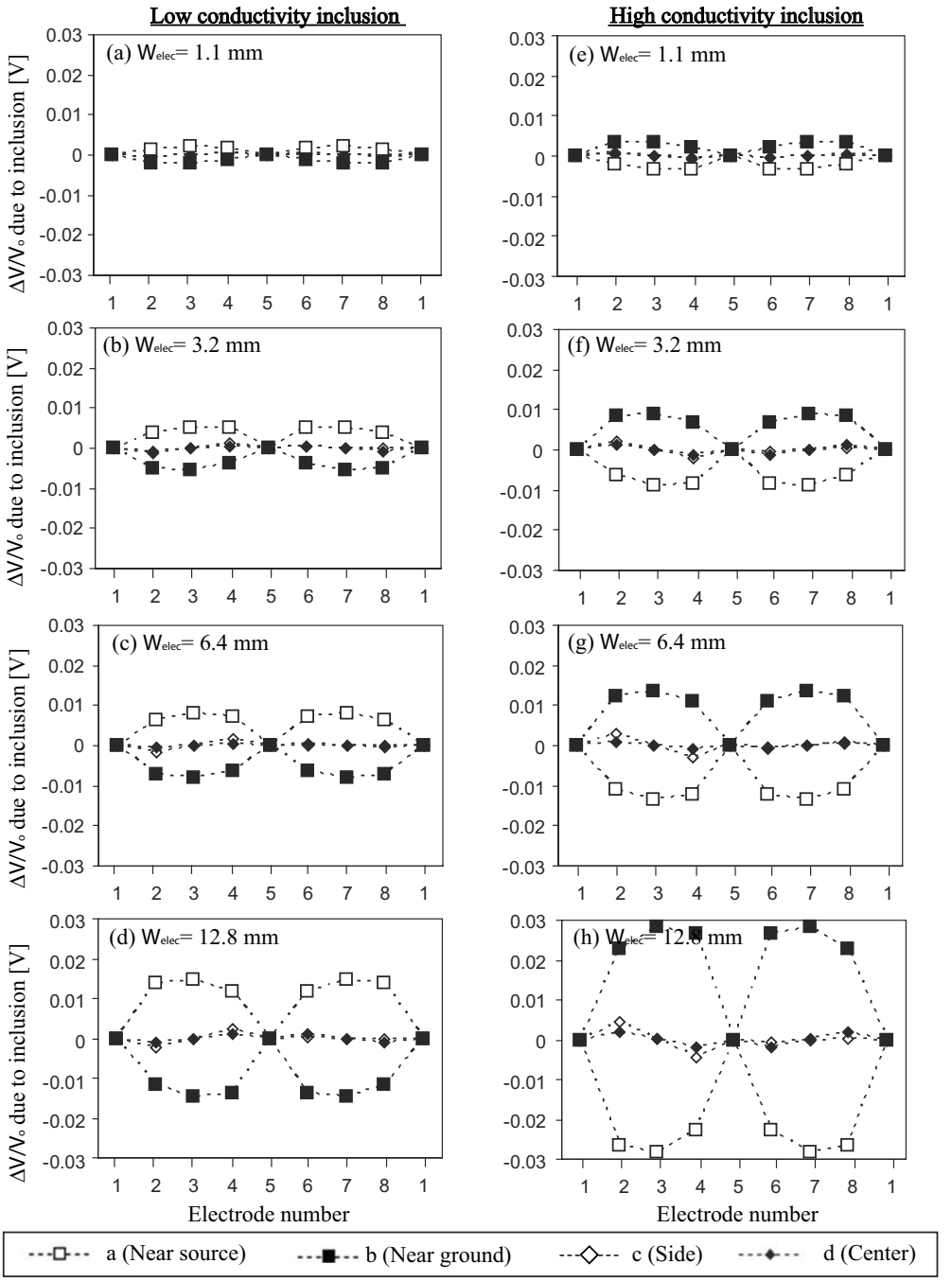

FIG. 8—*Signal strength produced by a spherical inclusion for half-cylindrical electrodes with varying widths. [(a)–(d)] Low conductivity inclusion. [(e)–(h)] High conductivity inclusion. Electrode length* $L_{elec}=7$ *mm; cell characteristics in Fig. 4; and inclusion specifications in Fig. 7.*

electrodes are placed around the perimeter to prevent shunting in which the current bypasses the medium and goes around the perimeter. Based on these results, we anticipate $W_{ele}/D_{cell} \approx \pi/2n$ for n-electrode configurations. In other words, the sum of the width of all electrodes should cover 50 % of the circumference.

Electrode Length

The preliminary study showed that similar to electrode width, electrode length also affects the strength of signals, which defines the ability of tomographic inversion to resolve the spatial distribution of conductivity in the medium (Fig. 3). A detailed numerical parametric study is conducted to explore electrode length effect on anomaly detection. Model conditions are described in Fig. 4. Simulations involve half-cylindrical electrodes ($W_{elec}/D_{cell} \approx 0.1$) of varying length between $L_{elec}=7$ mm and 50 mm. The spherical low conductivity inclusion ($\sigma_{inc}=0.05$ S/m) is either $D_{inc}=12$ mm or 24 mm in size and located at the center of the electrode plane in all cases (similar to Inc. d in Fig. 7).

Figure 10(*a*) shows the potential at electrodes 2 and 4 for a homogeneous medium versus electrode lengths. The potential difference between electrodes 2 and 4 increases as the electrode lengths

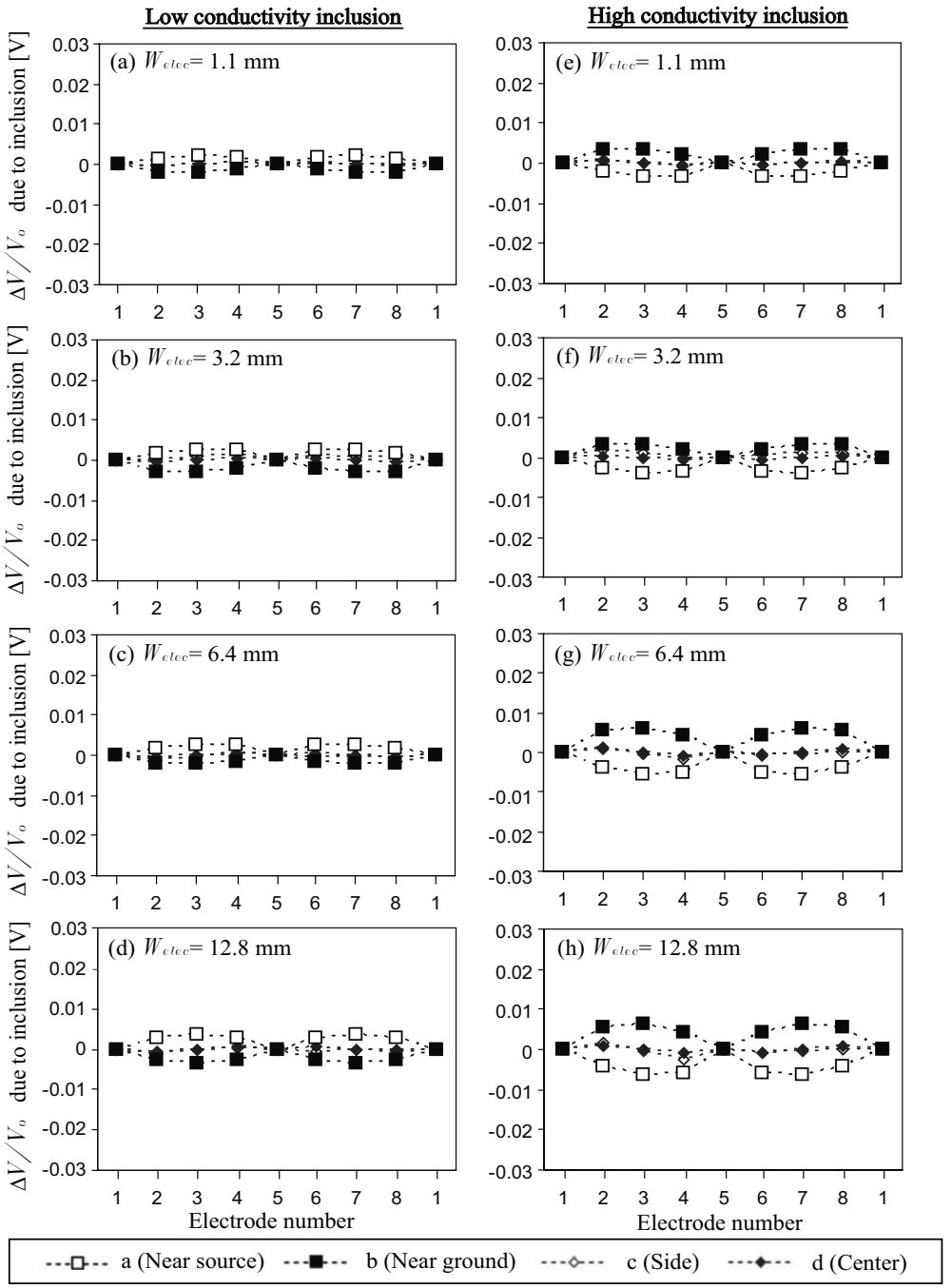

FIG. 9—*Signal strength produced by a spherical inclusion for flat electrodes with varying widths. [(a)–(d)] Low conductivity inclusion. [(e)–(h)] High conductivity inclusion. Electrode length L_{elec}= 7 mm; cell characteristics in Fig. 4; and inclusion specifications in Fig. 7.*

increase until the difference ΔV_{2-4} reaches an asymptote at $L_{\text{elec}} \approx 30$ mm ($L_{\text{elec}}/D_{\text{cell}} \approx 0.5$), suggesting that the electric field approaches a two-dimensional (2D) rather than a 3D condition. Figure 10(*b*) and 10(*c*) shows the signal strength in terms of potential change with respect to the homogeneous case $\Delta V/V_o$, measured at electrodes 2, 3, and 4 caused by the small and large low conductivity inclusions. The signal is less than $\Delta V/V_o \approx 0.002$ for the small-sized inclusion ($D_{\text{inc}}/D_{\text{cell}}$=0.2) and $\Delta V/V_o \approx 0.01$ for the large-sized inclusion ($D_{\text{inc}}/D_{\text{cell}}$=0.4). The response reaches a peak when the electrode length becomes $L_{\text{elec}} \approx 25$ mm ($L_{\text{elec}}/D_{\text{cell}} \approx 0.4$) for both D_{inc}=12 mm and D_{inc}=24 mm inclusions ($L_{\text{elec}}/D_{\text{inc}} \approx 2.1$ and 1.0). Combining results for homogeneous media and media with anomalies, we adopt an electrode length $L_{\text{elec}}/D_{\text{cell}} \approx 0.4$ for preliminary design.

Electrical Insulation

The electrical insulation between the specimen and the stainless steel cell is crucial for the implementation of ERT. While the cell wall can be electrically shielded with minor difficulties, top and bottom caps are more difficult to shield due to the inherent installation sequence and the presence of inlet and outlet ports for fluids and other sensors.

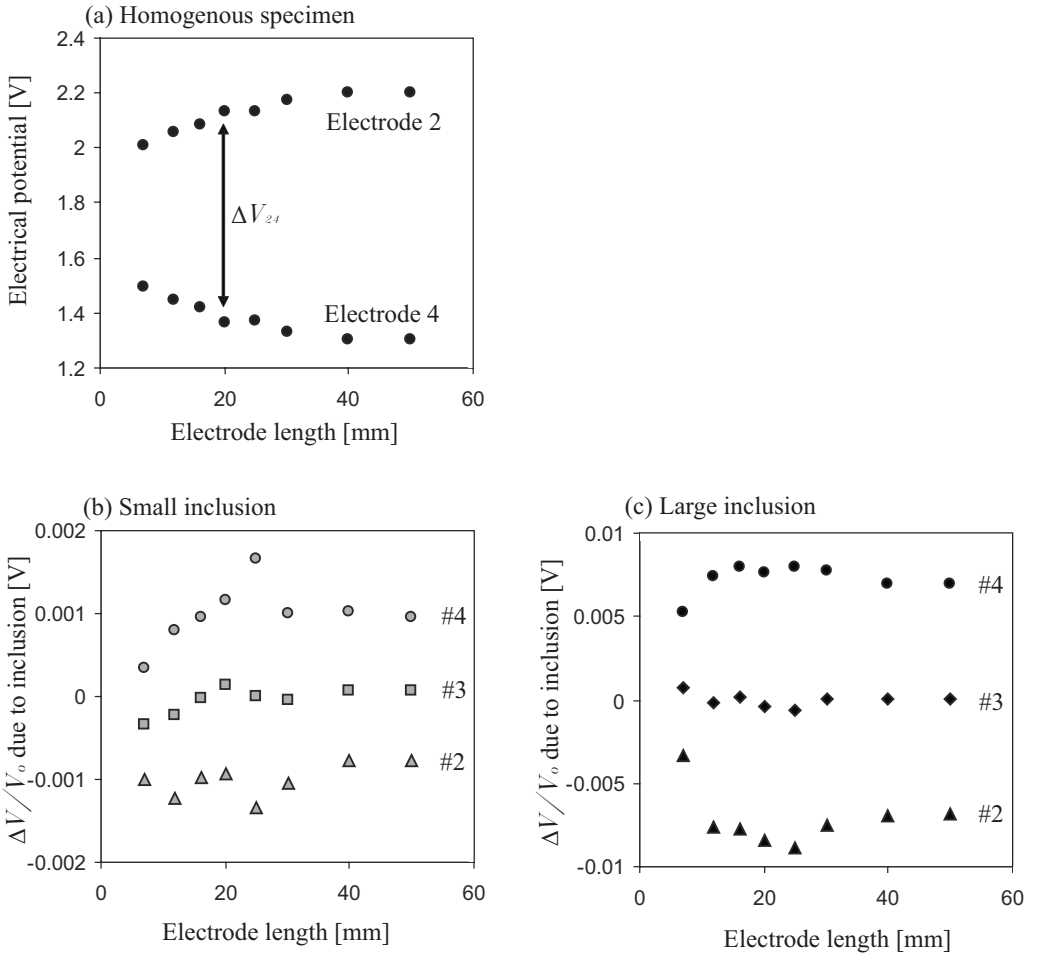

FIG. 10—*Electrode length effect—potential distribution and sensitivity to a low conductivity spherical inclusion at the center of the cell. (a) Potential at electrodes 2 and 4 in homogeneous specimen. Potential change with respect to homogeneous case induced by (b) small inclusion $D_{inc}=12$ mm and (c) large inclusion $D_{inc}=24$ mm. Model details in Fig. 4.*

The effect of partial shielding is numerically examined using the basic model specifications summarized in Fig. 4. Eight half-cylindrical electrodes are modeled ($W_{elec}=6.4$ mm and $L_{elec}=25$ mm). The three boundary conditions are simulated: Complete wall and end-caps insulation, wall insulation only, and no insulation. In the last case, we model a 1 mm gap filled with soil between electrodes and the wall to prevent short.

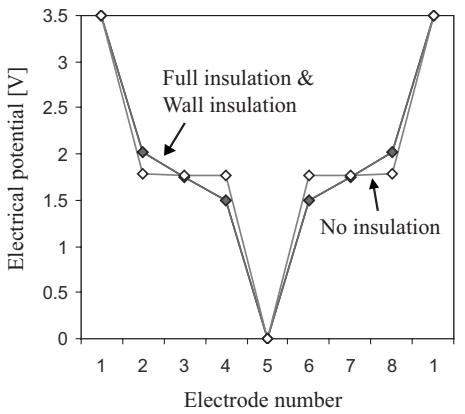

FIG. 11—*The effect of electrical insulation at the cell boundaries on the electrical potential distribution. Three cases: Complete wall and end-plates insulation, wall insulation, and no insulation (but with a 1 mm soil gap between electrodes and wall). Other model details in Fig. 4.*

Figure 11 shows the potential at all electrodes for different insulation conditions. The electrical potential in the non-insulated cell is homogeneous due to the concentrated current density along the wall, and no information can be gathered about the medium. Wall insulation (only) and complete insulation (wall and end caps) show almost the same results ($\Delta V/V_o \leq 0.009$). Therefore, the presence of a conductive surface at a distance $\delta/D_{cell} \geq 1$ does not affect measurements on the electrode plane.

The simulation is repeated with both low and high conductivity spherical inclusions ($\sigma_{inc}=0.05$ or 5 S/m and $\sigma_{sed}=0.5$ S/m) with diameter either $D_{inc}=12$ mm or 24 mm at the center of the electrode plane (similar to Inc. d in Fig. 7). Results shown in Fig. 12 confirm the previous conclusion: The presence of insulation at the top or bottom plates does not affect the performance of the ERT system in this cell configuration because most of the current flows in the plane of electrodes located at the center height when the distance from the electrode plane to the end-plates δ is similar to or exceeds the cell diameter, $\delta/D_{cell} \approx 1$.

Summary: Criteria for Electrical Resistivity Tomography Pre-Design

We examine potential and current density distribution in various ERT system configurations using both experimental and numerical

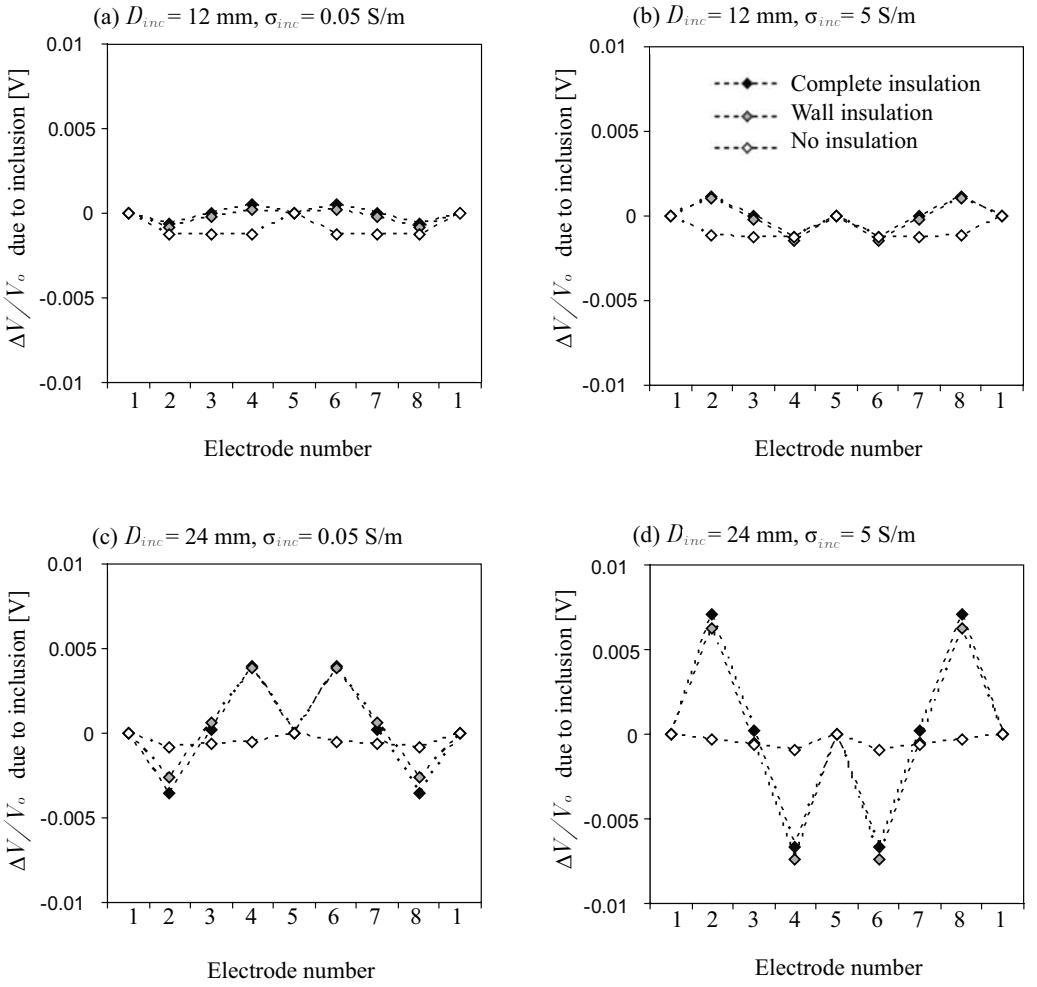

FIG. 12—*The effect of electrical insulation on anomaly detection. (a) D_{inc} = 12 mm and σ_{inc} = 0.05 S/m; (b) D_{inc} = 12 mm and σ_{inc} = 5 S/m; (c) D_{inc} = 24 mm and σ_{inc} = 0.05 S/m; (d) D_{inc} = 24 mm and σ_{inc} = 5 S/m. Other model details in Fig. 4.*

methods and explore optimal electrode configurations for cylindrical cells. Results show that optimal ERT configurations must take into consideration the required spatial resolution, sensitivity to anomalies, signal strength, and shunting effects along the cell perimeter.

The capacitive-type electrode polarization effect diminishes as the operating frequency increases, but it extends into higher frequencies as the conductivity of the electrolyte increases. The frequency sweep experiment in this study suggests that ERT measurements should be conducted at kHz frequencies for most soil applications in the absence of calibration data such as data from frequency sweep experiment.

When operating above the electrode polarization frequency, the high potential changes near source and sink electrodes are due to geometric Laplacian effects and lead to reduced signal strength in ERT applications. The study results mostly apply to one electrode plane system, which is 2D-ERT configuration but also can be adopted to the design of multi-electrode-plane system (3D-ERT configuration) with extra studies such as the distance between electrode planes. Study results suggest the following to mitigate the effect.

— The half-cylindrical electrode shape is convenient to reduce the geometric potential drop, and it is adequate for typical cylindrical cell configurations used in geotechnical studies.
— The potential drop can be reduced, and the response to the medium can be strengthened by using wider W_{elec} and longer L_{elec} electrodes at the expense of lower spatial resolution. However, the signal reaches an asymptote level for wide electrodes due to shunting and for long electrodes due to 3D → 2D transition.
— The following dimensionless ratios emerge as guidelines for preliminary design of n-electrode per plane 2D-ERT system configurations: $W_{elec}/D_{cell} \approx \pi/2n$ and $L_{elec}/D_{cell} \approx 0.4$.

Finally, end-cap insulation is not required in cylindrical cells when the distance between the electrode plane and conductive end caps exceeds $\delta/D_{cell} \geq 1$.

Acknowledgments

Support for this study was provided by the Chevron Joint Industry Project on Methane Hydrates from the U.S. Department of Energy. Additional support was provided by the Goizueta Foundation, KIGAM, GHDO, and MKE.

References

Avis, N. J. and Barber, D. C., 1994, "Image-Reconstruction Using Non-Adjacent Drive Configurations," *Physiol. Meas.*, Vol. 15,

pp. A153–A160.

Booth, M. J. and BasarabHorwath, I., 1996, "Comparing Electrode Configurations for Electrical Impedance Tomography," *Electron. Lett.*, Vol. 32(7), pp. 648–649.

Borsic, A., Comina, C., Foti, S., Lancellotta, R., and Musso, G., 2005, "Imaging Heterogeneities with Electrical Impedance Tomography: Laboratory Results," *Geotechnique*, Vol. 55(7), pp. 539–547.

Cohen-Bacrie, C., Goussard, Y., and Guardo, R., 1997, "Regularized Reconstruction in Electrical Impedance Tomography Using a Variance Uniformization Constraint," *IEEE Trans. Med. Imaging*, Vol. 16(5), pp. 562–571.

Comina, C., Foti, S., Musso, G., and Romero, E., 2008, "EIT Oedometer: An Advanced Cell to Monitor Spatial and Time Variability in Soil with Electrical and Seismic Measurements," *Geotech. Test. J.*, Vol. 31(5), pp. 1–9.

Dickin, F. and Wang, M. S., 1996, "Electrical Resistance Tomography for Process Applications," *Meas. Sci. Technol.*, Vol. 7 (3), pp. 247–260.

Huaxiang, W., Chao, W., and Wuliang, Y., 2001, "Optimum Design of the Structure of the Electrode for a Medical EIT System," *Meas. Sci. Technol.*, Vol. 12(8), pp. 1020–1023.

Klein, K. and Santamarina, J. C., 2003, "Electrical Conductivity in Soils: Underlying Phenomena," *J. Environ. Eng. Geophys.*, Vol. 8(4), pp. 263–273.

LaBrecque, D. J., Sharpe, E., Wood, T., and Heath, G., 2004, "Small-Scale Electrical Resistivity Tomography of Wet Fractured Rocks," *Ground Water*, Vol. 42(1), pp. 111–118.

Lyon, G. M. and Oakley, J. P., 1992, "Simulation Study of Sensitivity in Stirred Vessel Electrical Impedance Tomography," *Proceedings of a Workshop on Tomographic Techniques for Process Design and Operation*, Manchester, UK, March 26–29, Computational Mechanics Publ., Southampton, UK, p. 137.

Newell, J. C., Peng, Y., Edic, P. M., Blue, R. S., Jain, H., and Newell, R. T., 1998, "Effect of Electrode Size on Impedance Images of Two- and Three-Dimensional Objects," *IEEE Trans. Biomed. Eng.*, Vol. 45(4), pp. 531–534.

Pinheiro, P. A. T., Loh, W. W., and Dickin, F. J., 1998, "Optimal Sized Electrodes for Electrical Resistance Tomography," *Electron. Lett.*, Vol. 34(1), pp. 69–70.

Potts, B. D. and Santamarina, J. C., 1993, "Geotechnical Tomography. The Effects of Diffraction," *Geotech. Test. J.*, Vol. 16(4), pp. 510–517.

Santamarina, J. C. and Fratta, D. O., 2003, "Dynamic Energy Coupling—Electro-Seismic and Seismo-Electric Effects," *Transp. Porous Media*, Vol. 50(1–2), pp. 153–178.

Santamarina, J. C., Klein, K. A., and Fam, M. A., 2001, *Soils and Waves*, J. Wiley & Sons, New York, p. 488.

Seagar, A. D., Barber, D. C., and Brown, B. H., 1987, "Theoretical Limits to Sensitivity and Resolution in Impedance Imaging," *Clin. Phys. Physiol. Meas.*, Vol. 8, 13–31.

Zhou, Y. Q., Shimada, J., and Sato, A., 2001, "Three Dimensional Spatial and Temporal Monitoring of Soil Water Content Using Electrical Resistivity Tomography," *Water Resour. Res.*, Vol. 37, pp. 273–285.